



1 In addition, the shape of the grains seen in the AFM studies transformed from circular  
2 to triangular as the OFR was raised from 20 sccm to 30 sccm during an 800 °C  
3 thermal anneal. X-ray photoelectron spectroscopy was used to measure near-surface  
4 oxidation states of the thin-films with varying OFR in the annealing chamber. The  
5 bandgap energies were estimated from the ultra-violet and visible absorption spectra  
6 and low-temperature photoluminescence. An extracted bandgap value of 3.04 eV was  
7 determined for as-deposited CeO<sub>2</sub> films and this value increased with increasing  
8 annealing temperatures. However, no difference was observed in bandgap energies  
9 with variation of annealing atmosphere.

10  
11 **Keywords:** Post-deposition annealing; Magnetron sputtering, Ceria Microstructure; Grain  
12 Shape; XRD; XPS; UV absorption; Bandgap energy.

## 13 14 **HIGHLIGHTS**

- 15 • Deposition of ceria thin films by pulsed DC magnetron sputtering.
- 16 • Effect of annealing temperature and gas ambient on films crystalline structure.
- 17 • Evidence for control of the film roughness and grain size and shape are achieved.
- 18 • Investigation of the effect of post-deposition annealing on the film stoichiometry.
- 19 • Films showed blue shifts in bandgap energies with increasing annealing temperature.

## 20 21 **1. INTRODUCTION**

22 Cerium oxides (CeO<sub>2</sub>) have recently attracted much interest due to their chemical stability  
23 and unique chemical and physical properties, which make them suitable for many

1 applications [1]. The valence of the Ce ion is very important in determining the structure of  
2 cerium oxides; trivalent Ce forms the sesquioxide  $\text{Ce}_2\text{O}_3$ , which has a hexagonal lattice  
3 ( $P\bar{3}m1$  space group), while tetravalent Ce forms  $\text{CeO}_2$ , commonly known as ceria, which has  
4 a cubic fluorite lattice ( $Fm\bar{3}m$  space group) [2-4]. Thin films of the most common  $\text{CeO}_2$   
5 exhibit unique physical properties, such as a lattice constant similar to that of Si ( $a = 0.357$   
6 nm), a high refractive index and a high dielectric constant [5, 6]. Hence,  $\text{CeO}_2$  films are  
7 appropriate for many applications in optical devices [7, 8], microelectronic devices [9, 10],  
8 optoelectronic devices [11] and sensors [12]. They can also be utilised in other applications  
9 by effectively incorporating porosity between intermediate thin film layers to make thick  
10 porous structures. These further application areas include solar-thermal fuel generation [13],  
11 industrial catalysis [14, 15], solid oxide fuel cells [16] and oxidation prevention of human  
12 cells in biomedical devices [17].

13 Since  $\text{CeO}_2$  is stable even in sub-stoichiometric form ( $\text{CeO}_{2-\delta}$ ), it has been produced by  
14 several growth techniques including electron-beam evaporation [18], chemical vapour  
15 deposition [10], ion-beam-assisted deposition [19, 20], pulsed laser deposition [21] and  
16 reactive and non-reactive magnetron sputtering [6, 13]. However, magnetron sputtering is one  
17 of the most attractive techniques for the preparation of  $\text{CeO}_2$  films due to many advantages  
18 associated with the technique, including low substrate temperatures, scalability and good  
19 surface roughness characteristics [13], in addition to it being a well-established and relatively  
20 low cost industrial technique. Furthermore, the bipolar pulsed DC magnetron sputtering  
21 (PDCMS) process has attracted even greater attention recently because it shows higher  
22 deposition rates of defect-free ceramic films compared to conventional RF magnetron  
23 sputtering processes and therefore has potential as a commercially suitable method for large-  
24 area deposition of good quality ceramic films with high yield under diverse processing  
25 conditions [13].

1 According to various reports in the literature, highly crystalline CeO<sub>2</sub> can be obtained by  
2 applying heat to the substrate during deposition [22, 23]. However, this can also be achieved  
3 by post-deposition annealing of the CeO<sub>2</sub> film at high temperatures. Varying the substrate  
4 temperature during growth has an effect on the structural, chemical and optical properties but  
5 these effects are different to those obtained from varying oxygen flow rates (OFRs) during  
6 post-deposition annealing, especially in terms of microstructure (grain size and shape) of the  
7 films. Varying the post-deposition annealing temperature or the OFRs also results in changes  
8 in the concentration of oxygen vacancies, due to the altered thermodynamic equilibrium [24].  
9 These factors can also influence the structure and morphology of CeO<sub>2</sub> films [25-27], which  
10 play an important role in solid/solid catalysis and the electrical properties of CeO<sub>2</sub> [28, 29]  
11 Thus varying OFRs and temperature during post-deposition annealing offers potential for  
12 control and engineering of a thin film properties.

13 In this work, we characterise CeO<sub>2</sub> thin films grown on Si(100) and quartz substrates  
14 grown by PDCMS using a CeO<sub>2</sub> target. The influence of varying the OFR and post-  
15 deposition annealing temperature on the deposit characteristics (microstructure and  
16 morphology, composition, optical properties etc.) were studied. The films were analysed by  
17 x-ray diffraction (XRD), atomic force microscopy (AFM), x-ray photoelectron spectroscopy  
18 (XPS), ultraviolet-visible (UV-Vis) spectroscopy and low-temperature photoluminescence  
19 (LPL). The influence of the post-deposition anneal temperature and variation of the OFRs on  
20 the PDCMS CeO<sub>2</sub> films properties have not been reported previously, and our work provides  
21 useful information on the effects of temperature and variation of OFRs in terms of controlling  
22 thin film properties, specifically grain shape and size.

## 23 **2. EXPERIMENTAL**

### 24 **2.1. MATERIAL SYNTHESIS**

1 Nanostructured CeO<sub>2</sub> thin films were prepared by PDCMS of a CeO<sub>2</sub> target onto silicon  
2 and quartz substrates (2 × 2 cm). The target was 99.99% pure cerium oxide (50 mm diameter  
3 and 6 mm thickness, supplied by the Kurt J. Lesker Company). Prior to deposition, the  
4 substrates were ultrasonically cleaned using acetone, a decontamination solution (30905  
5 Aldrich), de-ionised water and blown dry with a nitrogen stream. An ENI RPG-100 pulse  
6 generator was used to drive a planar magnetron fitted with the CeO<sub>2</sub> target in power  
7 regulation mode. The chamber was first pumped down to a base pressure of 2 × 10<sup>-5</sup> Pa by  
8 cryogenic pumping. The target was pre-sputtered for 10 minutes prior to deposition to reduce  
9 target surface contamination and to obtain a stable plasma density. Sputtering was carried out  
10 in a pure Ar atmosphere and the working pressure was adjusted and maintained at 0.7 Pa for  
11 the duration of the deposition. The target to substrate distance was adjusted to 6 cm. The  
12 sputtering was done at room temperature using a power of 65 W at 150 kHz without  
13 intentional heating. The substrates were at floating potential and the sputtering time was  
14 adjusted to 60 minutes to obtain a uniform film thickness of 50 ± 10 nm for all the deposited  
15 samples.

## 16 **2.2. ANNEALING**

17 After deposition and a short contact time with air at room temperature, the CeO<sub>2</sub> thin  
18 films samples were transferred into a quartz glass cell, where annealing treatments were  
19 performed. Samples were ramped up to target temperatures of 500 °C, 800 °C and 1000 °C at  
20 a rate (*r*) of 40 °C min<sup>-1</sup> in an air ambient, and held at these temperatures for 1 hour (the dwell  
21 time, *t<sub>d</sub>*), in order to study the effect of annealing temperature on the film properties. An  
22 optimum temperature of 800 °C (*r* =40 °C min<sup>-1</sup>, *t<sub>d</sub>* = 1 hour) was chosen and further  
23 annealing experiments were carried out to study the effect of varying the oxygen partial  
24 pressure (p(O<sub>2</sub>)) during annealing on the PDCMS CeO<sub>2</sub> deposited films. This was done by  
25 heating CeO<sub>2</sub> thin films deposits in an Ar/O<sub>2</sub> atmosphere with various OFR values at 800 °C,

1 while keeping the argon flow rate (AFR) constant. The OFRs were varied in the range 0 – 50  
2 sccm. After 1 hour of annealing, the sample was allowed to cool down to room temperature  
3 (cooling time  $\approx$  30 min) before characterisation. Note that before each new annealing step,  
4 the gas atmosphere was refreshing by pumping and refilling.

5

### 6 **2.3. STRUCTURE AND MORPHOLOGY**

7 The structural properties of the sputtered CeO<sub>2</sub> films were measured using a Bruker D8  
8 advance x-ray diffractometer with CuK <sub>$\alpha$</sub>  radiation of wavelength  $\lambda = 1.54056 \text{ \AA}$  to determine  
9 the crystallinity of the films. The XRD measurements were carried out in locked-coupled ( $\theta$ -  
10  $2\theta$ ) mode in a  $2\theta$  range from  $20^\circ$  to  $60^\circ$ . A qualitative and quantitative phase analysis of the  
11 different phases was done by Rietveld analysis of the diffraction data using the FullProf  
12 program [30].

13 The surface morphology and roughness of the CeO<sub>2</sub> films were studied by a Veeco  
14 Nanoscope Dimension 3100 AFM instrument operating in tapping mode using aluminium-  
15 coated silicon (Si) probes (Budget Sensors, Tap300Al-G) with a tip radius of  $< 10 \text{ nm}$ . The  
16 intrinsic height resolution of the system is determined by the piezoelectric element and  
17 electronic noise and is  $\sim 0.4 \text{ nm}$ , which provides a base level for measurement reliability. The  
18 surface roughness of each sample was determined as the root mean square (RMS) value  $R_q$  of  
19 the distribution of heights in the AFM topography images. The row/column statistical tool of  
20 Gwyddion software was used to calculate the standard deviation of  $R_q$  of all individual  
21 row/column values, and the values obtained were considered when determining the roughness  
22 error bars [31]. Where the calculated standard deviation of all individual row/column values  
23 is greater than the intrinsic height resolution of the system, the standard deviation is used as

1 the error bar, and where it is less than the intrinsic height resolution, a value of 0.4 nm is used  
2 as the error bar.

## 3 **2.4. SPECTROSCOPY**

4 XPS analysis was carried out using a VG Microtech electron spectrometer with a base  
5 pressure of  $1 \times 10^{-7}$  Pa. The photoelectrons were excited with a conventional Mg  $K_{\alpha}$  ( $h\nu =$   
6  $1253.6$  eV) x-ray source and an electron energy analyser operating at a 20 eV pass energy,  
7 yielding an overall resolution of 1.2 eV. The samples were subjected to a mild degassing  
8 procedure in UHV at 300 °C in order to eliminate any surface contamination (this treatment  
9 was at too low a temperature to effect the properties being studied as a function of post  
10 deposition annealing), which may have arisen as a result of the transfer in atmosphere  
11 between the deposition and analysis chambers.

12 The optical absorption properties of the CeO<sub>2</sub> films were studied at room temperature  
13 using a Perkin Elmer Lambda 40 UV–Vis spectrometer in the range from 400 to 800 nm with  
14 a resolution of 4 nm. LPL measurements were carried out from 10 K to 22 K using a closed  
15 cycle helium cryostat system and a 325 nm excitation (He-Cd laser). The luminescence was  
16 analysed using a 1m grating spectrometer (SPEX 1704) with a photomultiplier tube  
17 (Hamamatsu model R3310-02) in photon counting mode and cooled to -20 °C by a Peltier  
18 cooler (EMI FACT50).

19

## 20 **3. RESULTS & DISCUSSIONS**

### 21 **3.1. STRUCTURE AND MORPHOLOGY**

22 Figure 1 shows a series of XRD  $\theta$ - $2\theta$  patterns from the CeO<sub>2</sub> thin films: as-deposited and  
23 post-deposition annealed at temperatures of 500 °C, 800 °C and 1000 °C for 1 h in an air  
24 ambient. As seen in figure 1, the as-deposited CeO<sub>2</sub> films show a broad and featureless XRD

1 pattern, characteristic of an amorphous structure. The CeO<sub>2</sub> films annealed at 500 °C shows  
2 the emergence of prominent diffraction peaks indexed to the cubic fluorite CeO<sub>2</sub> structure  
3 (PDF No. 00-034-0394), revealing that the CeO<sub>2</sub> films are being crystallized by the annealing  
4 process. For the films annealed at 800 °C and 1000 °C, we observe a higher intensity for the  
5 CeO<sub>2</sub> diffraction peaks which clearly reveals that the crystalline fraction of the CeO<sub>2</sub> films is  
6 improved upon increasing the annealing temperature. At these temperatures several weak  
7 diffraction peaks corresponding to the Ce<sub>2</sub>O<sub>3</sub> phase (PDF No. 00-049-1458) are also observed  
8 [32], possibly associated with the oxygen deficient growth environment (Ar gas only). These  
9 phases were further investigated using Rietveld refinement analysis of the CeO<sub>2</sub> diffraction  
10 patterns annealed at 500°C and 800°C and 1000°C (shown in figure 1) provided some  
11 temperature dependent phase change information, but the main conclusion is that the deposit  
12 is mainly composed of cubic CeO<sub>2</sub>, with some contribution from Ce<sub>2</sub>O<sub>3</sub> in all samples, very  
13 possibly with a degree of localisation at the surface when the XPS data in the manuscript is  
14 considered in conjunction with the XRD data and Rietveld analysis [33, 34]. The details of  
15 these impurity phases and their variation with annealing appears rather complex and, because  
16 of the evidence of surface localisation, further work will be needed to elucidate it more fully.  
17 Figure 2 shows the analysis for the CeO<sub>2</sub> for the three temperatures (500°C, 800°C and  
18 1000°C). To refine the different phases, the structure model (space groups) Fm3m was used  
19 for CeO<sub>2</sub>, CeO and Ce<sub>2</sub>O<sub>3</sub>, and P $\bar{3}$ m1 for Ce<sub>2</sub>O<sub>3</sub> (although no evidence of the CeO and  
20 hexagonal Ce<sub>2</sub>O<sub>3</sub>-phases were ultimately seen in the results of the refinement). Analysing the  
21 diffraction data it became obvious that some Ce<sub>2</sub>O<sub>3</sub> impurity phase occurs in the 800 °C and  
22 1000 °C samples, where there is evidence of the Ce<sub>2</sub>O<sub>3</sub> cubic type structure however, this  
23 phase is present only in smaller concentrations (wt.%) of 7.5, 6.6 and 8.1 for 500°C, 800°C  
24 and 1000°C, respectively. It can also be seen that the crystallinity deduced from the CeO<sub>2</sub>  
25 diffraction data improves with increasing temperature, by comparison of pattern (a) to (b) and

1 (c) in figure 2. As stated above there was no evidence for the presence of any CeO impurities  
2 in any of the samples. The ratio of  $R_{wp}/R_{exp}$ , referred to as the goodness of fit ( $\chi^2$ -factor) is  
3 reported in table 1. For all annealed samples, the  $\chi^2$ -factor is less than 1.5 indicating a high  
4 quality refinement [35]. However, in the XRD refinement of the samples annealed at 500 °C,  
5 not all peaks are well fitted/defined and this can be explained to be due to the fact that these  
6 samples contain both amorphous and crystalline fractions. Furthermore, the out of plane  
7 coherence length of the samples are reported in table 1, obtained using the Rietveld  
8 refinement analysis. We have checked a selection of the out of plane coherence length values  
9 extracted from the Rietveld refinement analysis against estimates using the Debye-Scherrer  
10 formula applied to the full width at half maximum (FWHM) of the CeO<sub>2</sub> (111) XRD peak  
11 and found excellent agreement in all cases.

12 A series of XRD patterns showing the effect of OFR variation during post-deposition  
13 annealing on the crystallinity of the CeO<sub>2</sub> films are shown in figure 3. The OFRs ranges from  
14 0 sccm to 50 sccm with a constant AFR of 50 sccm. The diffraction patterns for all samples  
15 are crystalline and clearly exhibit the presence of CeO<sub>2</sub> (111), (200), (220), (311) and (222)  
16 reflections. There are also weak diffraction peaks corresponding to the Ce<sub>2</sub>O<sub>3</sub> phase.

17 The FWHMs determined from the Rietveld analysis are used as a measure of the  
18 crystalline quality of the CeO<sub>2</sub> crystallites and are reported in table 2. As plotted in figure 4,  
19 the out of plane coherence length, based on the results from the Rietveld refinement analysis,  
20 decreases from 24 nm to 17 nm as the OFR increased from 0 sccm to 30 sccm, and increased  
21 to 24 nm as the OFR was raised further to 50 sccm. These values are all much less than the  
22 film thicknesses (which are constant in the range  $50 \pm 10$  nm as mentioned previously) and  
23 reveal a nanocrystalline deposit morphology. The oxygen content in the annealing chamber  
24 appears to have a small influence on the out of plane coherence length, which can also be

1 correlated to the AFM images shown in figure 5, assuming the crystallites are approximately  
2 equiaxed, but the variation is close to limit of resolution of our XRD system.

3         The surface morphologies of the samples are investigated using an AFM. The plan-  
4 view AFM images for the surfaces of the CeO<sub>2</sub> films are presented in figure 5 for as-  
5 deposited films and films annealed at 800 °C in various OFRs (0 sccm, 20 sccm, 30 sccm and  
6 50 sccm). As can be seen in figure 5(a), the as-deposited amorphous CeO<sub>2</sub> films have a very  
7 smooth and uniform surface. However, the surface morphology roughens after annealing at  
8 800 °C, due to the crystallisation of the amorphous CeO<sub>2</sub> films. For samples annealed in  
9 OFRs of 0 sccm and 20 sccm (figure 5 b and c), the shape of the CeO<sub>2</sub> grains is roughly  
10 circular and the RMS roughness values were  $3.2 \pm 1.2$  nm to  $2.5 \pm 0.8$  nm, respectively. By  
11 contrast, the grain shape for the samples annealed in OFRs of 30 sccm to 50 sccm (figure 5 d  
12 and e) is triangular in nature and the RMS roughness increased from  $1.0 \pm 0.4$  nm to  $5.2 \pm 2.0$   
13 nm. The RMS roughness values (nm) of the films for a  $2 \times 2 \mu\text{m}^2$  scan area are summarized in  
14 table 2. For comparison, the as-deposited CeO<sub>2</sub> film RMS roughness is very smooth (at or  
15 below the intrinsic height resolution of the system, 0.4 nm).

16

### 17 **3.2. CHEMICAL COMPOSITION STUDIES USING XPS**

18 The chemical compositions of the films were studied by XPS in order to probe the presence  
19 of Ce<sup>4+</sup> and Ce<sup>3+</sup> oxidation states and their relative concentrations. Figure 6 displays the Ce3d  
20 core level spectra of the as-deposited sample and samples annealed at 800 °C for 60 minutes  
21 in different OFRs. There was no significant effect from varying the OFRs in the annealing  
22 chamber. The established binding energy positions of the Ce<sup>3+</sup> and Ce<sup>4+</sup> oxidation state [36]  
23 are indicated by the vertical dotted lines [13]. The spectrum clearly shows a higher  
24 concentration of Ce in the Ce<sup>3+</sup> oxidation state in the as-deposited sample compared to those  
25 annealed at 800 °C in gas, indicating a chemically reduced state of CeO<sub>2</sub> possibly associated

1 with the oxygen deficient growth environment (Ar gas only). Thus the as-deposited CeO<sub>2</sub>  
2 sample shows a mixed phase Ce<sup>3+</sup>/Ce<sup>4+</sup> charge state, while the annealed CeO<sub>2</sub> samples in 0  
3 sccm and 50 sccm OFRs are solely due to Ce<sup>4+</sup> (within the limits of sensitivity of our  
4 system). It should be noted that although the presence of Ce<sup>3+</sup> and Ce<sup>4+</sup> could easily be  
5 identified in the Ce 3d as-deposited spectra, the relative concentrations could not be  
6 determined due to the complexity of the peak shape and the difficulty in fitting the peak.

7 Figure 7 shows the corresponding O 1s XPS data for the as-deposited CeO<sub>2</sub> and CeO<sub>2</sub>  
8 annealed samples. The binding energy positions of the various Ce oxidation states in the O 1s  
9 core level spectra are almost identical and overlap considerably [37], mainly due to the O<sup>2-</sup>  
10 nature of the oxygen atom in both Ce<sub>2</sub>O<sub>3</sub> and CeO<sub>2</sub>. These two contributions give rise to the  
11 feature labelled (i) in figure 7 and consequently, it is very difficult to deconvolve the O 1s  
12 peak into Ce<sub>2</sub>O<sub>3</sub> and CeO<sub>2</sub> components. However, by assuming that the O 1s peak is in a  
13 single CeO<sub>2</sub> phase at the surface of the annealed samples due to the absence of a Ce<sup>3+</sup>  
14 oxidation state in the Ce 3d data in figure 6, it was possible to establish peak fitting  
15 parameters for the O 1s CeO<sub>2</sub> Ce<sup>4+</sup> component. These parameters were used to fit the O 1s  
16 spectrum for the as-deposited sample, where both Ce<sup>3+</sup> and Ce<sup>4+</sup> states exist as shown in the  
17 Ce 3d spectra in figure 6. It was evident that an additional peak was needed to achieve an  
18 adequate fit and it is suggested that this additional peak is due to the Ce<sup>3+</sup> oxidation state and  
19 is separated from the Ce<sup>4+</sup> by ~0.3eV in agreement with Mullins et al. [38]. Using these  
20 parameters the relative concentrations of the Ce<sup>3+</sup> : Ce<sup>4+</sup> as determined by the O 1s core level  
21 spectra in the as-deposited film is roughly 1 : 1.

22 The presence of OH groups or C-O contamination on the surface have previously been  
23 discussed as possible explanations for the feature labelled (ii) in figure 7, at a binding energy  
24 ~ 1.8eV higher than that of the Ce<sup>4+</sup> oxidation state in the O 1s spectrum [37, 38]. Samples  
25 with exposure to different OFR conditions and samples annealed at a temperature of 800 °C

1 contain larger relative contributions (up to ~31% of the signal in this spectral region) from  
2 these contaminant species. As stated above, the annealed samples, regardless of OFR, show  
3 evidence of Ce in the  $Ce^{4+}$  oxidation state only and a higher percentage of the contaminant  
4 feature (ii).

5 In figure 8, the annealed  $CeO_2$  samples were further investigated by performing an off-  
6 normal emission scan. The scan indicated that the contaminant species O-H/C-O are indeed  
7 surface localised, as expected, and are most likely due to atmospheric exposure. All the  
8 samples were exposed to atmosphere at room temperature for a short period; thus it is  
9 possible that the surfaces of all samples were more heavily oxidised in contrast to the bulk at  
10 least within the sampling depth of the XPS, and especially so for the case of some of the  
11 annealed samples. Lohwasser et al. [39] described an inward diffusion process of  $O_2$  into  
12  $CeO_2$  sputtered films in the temperature range from 700 °C to 950 °C which results in  $CeO_\delta$   
13 material being surface localised, however due to the proximity of the various oxidation states  
14 in the O 1s spectra, it is very difficult to verify these findings using XPS in this study.

15 In summary, XPS indicates that the surface of the as-deposited film consisted of a  $Ce^{3+}/Ce^{4+}$   
16 mixed phase, while the annealed sample surfaces appeared to contain just the  $Ce^{4+}$  oxidation  
17 state which is consistent with a more heavily oxidised surface for the annealed samples. It  
18 should be noted that XPS is extremely surface sensitive and its findings do not generally  
19 accurately reflect bulk properties. Nevertheless these XPS data are consistent with the XRD  
20 data and Rietveld refinement analysis above which show evidence only for  $Ce_2O_3$  and  $CeO_2$   
21 phases, as XPS data from all samples shows the presence of only the  $Ce^{4+}$  and  $Ce^{3+}$  oxidation  
22 states (and no evidence for the  $Ce^{2+}$  charge state, associated with the CeO phase, which was  
23 not seen in XRD), though the relative concentrations indicated by XRD and XPS cannot be  
24 compared for the reason alluded to above.

1

### 2 **3.3. UV ABSORPTION AND BANDGAP ENERGY**

3 It was previously reported [40-42] that a change in particle size due to exposure to different  
4 temperatures leads to a shift of absorption edge in UV-Vis absorption spectra. Figure 9 shows  
5 the UV-Vis data from our samples, and the data indicates that the absorption edge shifts  
6 toward shorter wavelengths i.e. a blue shift, despite the increase in crystal size, with  
7 increasing post-deposition annealing temperature. The direct bandgap energy was estimated  
8 by extrapolating the absorption coefficient ( $\alpha$ ) from the absorbance data using a Tauc plot.

9 From the Tauc plot of  $(\alpha h\nu)^2$  versus  $h\nu$  (figure 10), one clearly sees that the extracted  
10 bandgap value increases from 3.3 eV to 3.6 eV as the annealing temperature increases from  
11 500 °C to 1000 °C. For comparison the extracted bandgap value is 3.04 eV for as-deposited  
12 CeO<sub>2</sub> films. No changes were observed when the OFR was varied in the annealing chamber  
13 compared to the data from a sample annealed at 800 °C in air. The physical meaning of the  
14 extracted values and their variation with process conditions must however be treated with  
15 caution, because the influence of excitonic effects, as well as Urbach tail effects, on the  
16 spectra is not clear, and it is known that such effects are not accounted for within the Tauc  
17 plot formalism [43].

18

### 19 **3.4. Photoluminescence**

20 Low temperature photoluminescence was performed on nanocrystalline CeO<sub>2</sub> films annealed  
21 at 800°C in various OFRs. All nanocrystalline CeO<sub>2</sub> samples displayed similar LPL spectra to  
22 that shown in figure 11, so only the data for a sample annealed in an OFR of 50 sccm is  
23 shown. It can be clearly seen that the peak intensity at 3.36 eV increases with increasing LPL  
24 measurement temperature. This behaviour indicates that the 3.36 eV emissions are associated

1 with the films (unlike the laser plasma line at  $\sim 3.43$  eV which doesn't vary with  
2 temperature). The emission at 3.36 eV is associated with near bandedge emission from the  
3 film material and correlates well with the known value of the CeO<sub>2</sub> bandgap at room  
4 temperature (3.2 eV) [44, 45], albeit being slightly larger due to the cryogenic measurement  
5 temperatures and associated bandgap increase. From our LPL data it does not appear that the  
6 bandgap is significantly affected by the OFR value during the annealing treatment, consistent  
7 with the UV-Vis data mentioned earlier.

8

#### 9 **4. CONCLUSIONS**

10 From the results presented above, the crystalline structure and morphology of CeO<sub>2</sub> thin films  
11 deposited by PDCMS are strongly dependent on the post-deposition annealing temperature  
12 and OFR of the Ar/O<sub>2</sub> annealing atmosphere. The average grain size can be controlled by  
13 either varying the annealing temperature or the OFR during the thermal anneal process.  
14 Raising the OFR from 20 sccm to 30 sccm resulted in the grain shape changing from roughly  
15 circular to triangular. Analysis of the chemical composition showed that the surfaces of the  
16 as-deposited films had contributions from both Ce<sup>3+</sup> and Ce<sup>4+</sup> charge states while the  
17 annealed CeO<sub>2</sub> films had contributions predominantly from the Ce<sup>4+</sup> charge state and this  
18 charge state dominated at the film surface. These data are consistent with XRD data and  
19 Rietveld refinement analysis. The thermal anneal temperature also plays an important role in  
20 the optical properties of the films where an increase in temperature leads to a blue-shift and  
21 an increase in the bandgap value.

22 Our data and analysis clearly show that key materials properties such as the film  
23 nanomorphology, bandgap value and Ce ion charge state can be varied by a suitable thermal  
24 annealing treatment. These results may prove very useful in terms of enabling future

1 materials and device development, with the aim of controlling key film parameters for  
2 technologically important applications, in particular in the areas of solar-thermal fuel  
3 generation and catalysis.

4

## 5 **ACKNOWLEDGEMENTS**

6 A. Eltayeb, S. Daniels and E. McGlynn specifically acknowledge postgraduate funding  
7 support from the INSPIRE programme funded under the framework of the Irish government's  
8 PRTLII cycle 5, National Development Plan 2007-2014 with the assistance of the European  
9 regional development fund.

10

## 11 **REFERENCES**

- 12 [1] Y. Kuru, S. Bishop, J. Kim, B. Yildiz, H. Tuller, Chemomechanical properties and  
13 microstructural stability of nanocrystalline Pr-doped ceria: An *in situ* X-ray  
14 diffraction investigation, Solid State Ionics, 193 (2011) 1-4.
- 15 [2] L. Wu, H. Wiesmann, A. Moodenbaugh, R. Klie, Y. Zhu, D. Welch, M. Suenaga,  
16 Oxidation state and lattice expansion of CeO<sub>2-x</sub> nanoparticles as a function of particle size,  
17 physical review B, 69 (2004) 125415.
- 18 [3] E. Rossinyol, J. Arbiol, F. Peiró, A. Cornet, J. Morante, B. Tian, T. Bo, D. Zhao,  
19 Nanostructured metal oxides synthesized by hard template method for gas sensing  
20 applications, Sensors and Actuators B: Chemical, 109 (2005) 57-63.
- 21 [4] N. Skorodumova, R. Ahuja, S. Simak, I. Abrikosov, B. Johansson, B. Lundqvist,  
22 Electronic, bonding, and optical properties of CeO<sub>2</sub> and Ce<sub>2</sub>O<sub>3</sub> from first principles,  
23 Physical Review B, 64 (2001) 115108.

- 1 [5] N. Savvides, A. Thorley, S. Gnanarajan, A. Katsaros, Epitaxial growth of cerium oxide  
2 thin film buffer layers deposited by dc magnetron sputtering, *Thin Solid Films*, 388 (2001)  
3 177-182.
- 4 [6] M.-T. Ta, D. Briand, Y. Guhel, J. Bernard, J. Pesant, B. Boudart, Growth and structural  
5 characterization of cerium oxide thin films realized on Si (111) substrates by on-axis rf  
6 magnetron sputtering, *Thin Solid Films*, 517 (2008) 450-452.
- 7 [7] R.P. Netterfield, W.G. Sainty, P.J. Martin, S.H. Sie, Properties of  $\text{CeO}_2$   
8 thin films prepared by oxygen-ion-assisted deposition, *Applied optics*, 24 (1985) 2267-2272.
- 9 [8] G. Atanassov, R. Thielsch, D. Popov, Optical properties of  $\text{TiO}_2$ ,  $\text{Y}_2\text{O}_3$  and  $\text{CeO}_2$   
10 thin films deposited by electron beam  
11 evaporation, *Thin Solid Films*, 223 (1993) 288-292.
- 12 [9] T. Ami, M. Suzuki, MOCVD growth of (100)-oriented  $\text{CeO}_2$  thin films on  
13 hydrogen-terminated Si (100) substrates, *Materials Science and Engineering: B*, 54 (1998)  
14 84-91.
- 15 [10] D. Norton, J. Budai, M. Chisholm, Hydrogen-assisted pulsed-laser deposition of (001)  
16  $\text{CeO}_2$  on (001) Ge, *Applied Physics Letters*, 76 (2000) 1677-1679.
- 17 [11] A. Morshed, M. Moussa, S. Bedair, R. Leonard, S. Liu, N. El-Masry, Violet/blue  
18 emission from epitaxial cerium oxide films on silicon substrates, *Applied physics letters*, 70  
19 (1997) 1647-1649.
- 20 [12] P. Jasinski, T. Suzuki, H.U. Anderson, Nanocrystalline undoped ceria oxygen sensor,  
21 *Sensors and Actuators B: Chemical*, 95 (2003) 73-77.
- 22 [13] A. Eltayeb, R.K. Vijayaraghavan, A. McCoy, A. Venkatanarayanan, A.A. Yaremchenko,  
23 R. Surendran, E. McGlynn, S. Daniels, Control and enhancement of the oxygen storage  
24 capacity of ceria films by variation of the deposition gas atmosphere during pulsed DC  
25 magnetron sputtering, *Journal of Power Sources*, 279 (2015) 94-99.

- 1 [14] A. Trovarelli, C. de Leitenburg, M. Boaro, G. Dolcetti, The utilization of ceria in  
2 industrial catalysis, *Catalysis today*, 50 (1999) 353-367.
- 3 [15] T.X. Sayle, S.C. Parker, D.C. Sayle, Oxidising CO to CO<sub>2</sub> using ceria nanoparticles,  
4 *Physical Chemistry Chemical Physics*, 7 (2005) 2936-2941.
- 5 [16] B.C. Steele, A. Heinzl, Materials for fuel-cell technologies, *Nature*, 414 (2001) 345-  
6 352.
- 7 [17] M.S. Wason, J. Colon, S. Das, S. Seal, J. Turkson, J. Zhao, C.H. Baker, Sensitization of  
8 pancreatic cancer cells to radiation by cerium oxide nanoparticle-induced ROS production,  
9 *Nanomedicine: Nanotechnology, Biology and Medicine*, 9 (2013) 558-569.
- 10 [18] M. Anwar, S. Kumar, F. Ahmed, N. Arshi, Y.J. Seo, C.G. Lee, B.H. Koo, Study of  
11 nanocrystalline ceria thin films deposited by e-beam technique, *Current Applied Physics*, 11  
12 (2011) S301-S304.
- 13 [19] D. Huang, F. Qin, Z. Yao, Z. Ren, L. Lin, W. Gao, Q. Ren, High quality CeO<sub>2</sub> film  
14 grown on Si (111) substrate by using low energy dual ion beam deposition technology,  
15 *Applied physics letters*, 67 (1995) 3724-3725.
- 16 [20] Y.M. Chiang, E. Lavik, I. Kosacki, H. Tuller, J. Ying, Defect and transport properties of  
17 nanocrystalline CeO<sub>2-x</sub>, *Applied Physics Letters*, 69 (1996) 185-187.
- 18 [21] T. Chikyow, S. Bedair, L. Tye, N. El-Masry, Reaction and regrowth control of CeO<sub>2</sub> on  
19 Si (111) surface for the silicon-on-insulator structure, *Applied physics letters*, 65 (1994)  
20 1030-1032.
- 21 [22] K.N. Rao, L. Shivlingappa, S. Mohan, Studies on single layer CeO<sub>2</sub> and SiO<sub>2</sub> films  
22 deposited by rotating crucible electron beam evaporation, *Materials Science and Engineering:*  
23 *B*, 98 (2003) 38-44.

- 1 [23] A. Khare, R. Choudhary, K. Bapna, D. Phase, S.P. Sanyal, Resonance photoemission  
2 studies of (111) oriented CeO<sub>2</sub> thin film grown on Si (100) substrate by pulsed laser  
3 deposition, *Journal of Applied Physics*, 108 (2010) 103712.
- 4 [24] V.F. Solovyov, T. Ozaki, A. Atrei, L. Wu, A. Al-Mahboob, J.T. Sadowski, X. Tong, D.  
5 Nykypanchuk, Q. Li, Highly efficient solid state catalysis by reconstructed (001) Ceria  
6 surface, *Scientific reports*, 4 (2014).
- 7 [25] G. Chiodelli, L. Malavasi, V. Massarotti, P. Mustarelli, E. Quartarone, Synthesis and  
8 characterization of Ce<sub>0.8</sub>Gd<sub>0.2</sub>O<sub>2-y</sub>  
9 polycrystalline and thin film materials, *Solid State Ionics*, 176 (2005) 1505-1512.
- 10 [26] H. Fukuda, M. Miura, S. Sakuma, S. Nomura, Structural and electrical properties of  
11 crystalline CeO<sub>2</sub> films formed by metalorganic decomposition, *Japanese journal of applied*  
12 *physics*, 37 (1998) 4158.
- 13 [27] J.-H. Yoo, S.-W. Nam, S.-K. Kang, Y.-H. Jeong, D.-H. Ko, J.-H. Ku, H.-J. Lee, A study  
14 on the microstructure and electrical properties of CeO<sub>2</sub> thin films for gate  
15 dielectric applications, *Microelectronic engineering*, 56 (2001) 187-190.
- 16 [28] T. Suzuki, I. Kosacki, H.U. Anderson, Microstructure–electrical conductivity  
17 relationships in nanocrystalline ceria thin films, *Solid State Ionics*, 151 (2002) 111-121.
- 18 [29] P. Miceli, S. Bensaid, N. Russo, D. Fino, CeO<sub>2</sub>-based catalysts with engineered  
19 morphologies for soot oxidation to enhance soot-catalyst contact, *Nanoscale research letters*,  
20 9 (2014) 1-10.
- 21 [30] S. Schorr, A. Weber, V. Honkimäki, H.-W. Schock, In-situ investigation of the kesterite  
22 formation from binary and ternary sulphides, *Thin Solid Films*, 517 (2009) 2461-2464.
- 23 [31] A.A. Duarte, S.L. Filipe, L.M. Abegão, P.J. Gomes, P.A. Ribeiro, M. Raposo,  
24 Adsorption kinetics of DPPG liposome layers: a quantitative analysis of surface roughness,  
25 *Microscopy and Microanalysis*, 19 (2013) 867-875.

- 1 [32] J. Hanawalt, H. Rinn, L. Frevel, Chemical analysis by X-ray diffraction, Industrial &  
2 Engineering Chemistry Analytical Edition, 10 (1938) 457-512.
- 3 [33] C. Hardacre, G.M. Roe, R.M. Lambert, Structure, composition and thermal properties of  
4 cerium oxide films on platinum {111}, Surface science, 326 (1995) 1-10.
- 5 [34] S. Eck, C. Castellarin-Cudia, S. Surnev, M. Ramsey, F. Netzer, Growth and thermal  
6 properties of ultrathin cerium oxide layers on Rh (111), Surface science, 520 (2002) 173-185.
- 7 [35] R.A. Young, The rietveld method, Crystal research and technology, 30 (1995).
- 8 [36] L. Garvie, P. Buseck, Determination of  $Ce^{4+}/Ce^{3+}$  in  
9 electron-beam-damaged  $CeO_2$  by electron energy-loss spectroscopy, Journal  
10 of Physics and Chemistry of solids, 60 (1999) 1943-1947.
- 11 [37] H. Borchert, Y.V. Frolova, V.V. Kaichev, I.P. Prosvirin, G.M. Alikina, A.I.  
12 Lukashevich, V.I. Zaikovskii, E.M. Moroz, S.N. Trukhan, V.P. Ivanov, Electronic and  
13 chemical properties of nanostructured cerium dioxide doped with praseodymium, The Journal  
14 of Physical Chemistry B, 109 (2005) 5728-5738.
- 15 [38] D. Mullins, S. Overbury, D. Huntley, Electron spectroscopy of single crystal and  
16 polycrystalline cerium oxide surfaces, Surface Science, 409 (1998) 307-319.
- 17 [39] W. Lohwasser, J. Gerblinger, U. Lampe, H. Meixner, Effect of grain size of sputtered  
18 cerium-oxide films on their electrical and kinetic behavior at high temperatures, Journal of  
19 applied physics, 75 (1994) 3991-3999.
- 20 [40] H.-I. Chen, H.-Y. Chang, Synthesis of nanocrystalline cerium oxide particles by the  
21 precipitation method, Ceramics International, 31 (2005) 795-802.
- 22 [41] C. Liu, Z. Xu, Y. Zhang, J. Fu, S. Zang, Y. Zuo, Effect of annealing temperature on  
23 properties of ZnO: Al thin films prepared by pulsed DC reactive magnetron sputtering,  
24 Materials Letters, 139 (2015) 279-283.

- 1 [42] P. Patsalas, S. Logothetidis, L. Sygellou, S. Kennou, Structure-dependent electronic  
2 properties of nanocrystalline cerium oxide films, *Physical Review B*, 68 (2003) 035104.
- 3 [43] C.F. Klingshirn, *Semiconductor optics*, Springer Science & Business Media, 2012.
- 4 [44] A. Corma, P. Atienzar, H. Garcia, J.-Y. Chane-Ching, Hierarchically mesostructured  
5 doped CeO<sub>2</sub> with potential for solar-cell use, *Nature materials*, 3 (2004) 394-397.
- 6 [45] Z.C. Orel, B. Orel, Optical properties of pure CeO<sub>2</sub> and mixed CeO<sub>2</sub>/SnO<sub>2</sub> thin film  
7 coatings, *physica status solidi (b)*, 186 (1994) K33-K36.
- 8

Table 1 Rietveld refinement goodness of fit values and out of plane coherence length for CeO<sub>2</sub> samples annealed at 500 °C, 800 °C and 1000 °C.

Annealing Temperature (°C)	Out of plane coherence length (nm)	Goodness of fit values ( $\chi^2$ )
500	8	1.13
800	11	1.15
1000	19	1.23

Table 2 Summary of post-deposition annealing AFM and XRD results with variation in OFR. Samples were annealed at 800 °C for 1 hour.

Sample	OFR (sccm)	FWHM (°)	Out of Plane Coherence Length (nm)	RMS Roughness (nm)	Grain Shape
(a)	0	<u>0.38</u>	<u>24</u>	<u>3.2 ± 1.2</u>	Circular
(b)	10	<u>0.38</u>	<u>24</u>	<u>2.8 ± 0.4</u>	Circular
(c)	20	<u>0.43</u>	<u>21</u>	<u>2.5 ± 0.8</u>	Circular
(d)	30	<u>0.53</u>	<u>17</u>	<u>1.0 ± 0.4</u>	Triangular
(e)	40	<u>0.46</u>	<u>20</u>	<u>2.3 ± 0.6</u>	Triangular
(f)	50	<u>0.38</u>	<u>24</u>	<u>5.2 ± 2.0</u>	Triangular

Figure 1 XRD  $\theta$ - $2\theta$  patterns of the CeO<sub>2</sub> films, (a) as-deposited and post-deposition annealed at temperatures of (b) 500 °C, (c) 800 °C and (d) 1000 °C in an air ambient.

Figure 2 Rietveld analysis of three diffraction patterns of CeO<sub>2</sub> annealed samples. a) 500 °C anneal, b) 800 °C anneal and c) 1000 °C anneal. The refinement of data was obtained using three different phases (CeO<sub>2</sub>, Ce<sub>2</sub>O<sub>3</sub>; order corresponds to indicated Bragg peak positions from first to second line and we note that no evidence of the CeO phase is seen).

Figure 3 XRD patterns of nanostructured CeO<sub>2</sub> thin films grown on Si(100) substrates. The films were annealed at 800 °C, with various (a) 0 sccm, (b) 10 sccm, (c) 20 sccm, (d) 30 sccm, e) 40 sccm and (f) 50 sccm.

Figure 4 Influence of OFR during post-deposition annealing on the out of plane coherence length of the CeO<sub>2</sub> films.

Figure 5 2 x 2  $\mu\text{m}^2$  plan-view AFM images of nanostructured CeO<sub>2</sub> films: (a) as-deposited and post-deposition annealed at 800 °C in an OFR of (b) 0 sccm, (c) 20 sccm, (d) 30 sccm and (e) 50 sccm. The AFR is kept constant at 50 sccm for all samples.

Figure 6 XPS Ce3d core level spectra for a) as-deposited CeO<sub>2</sub> and 800 °C annealed CeO<sub>2</sub> samples with OFRs of b) 0 sccm and c) 50 sccm. The brackets show the spin orbital pairs (5/2) and (3/2) for Ce<sup>4+</sup> (solid lines) and Ce<sup>3+</sup> (dashed lines).

Figure 7 O 1s XPS spectra of CeO<sub>2</sub> samples: a) as-deposited, and annealed at 800 °C in an OFR of b) 0 sccm and c) an OFR of 50 sccm.

Figure 8 O 1s XPS spectra of 800 °C thermal annealed CeO<sub>2</sub> sample (the data shown is from a sample annealed at an OFR value of 50 sccm, but essentially the same spectra and behaviour were seen regardless of OFR value for all samples annealed at 800 °C), normal emission and off-normal emission.

Figure 9 UV-Vis absorption spectra of CeO<sub>2</sub> sputtered films, as-deposited and post-deposition annealed at temperatures of 500 °C, 800 °C and 1000 °C in an air ambient.

Figure 10 Tauc plot of  $(\alpha h\nu)^2$  vs.  $h\nu$  for nanostructured CeO<sub>2</sub> sputtered films, as-deposited and post-deposition annealed at temperatures of 500 °C, 800 °C and 1000 °C in an air ambient.

Figure 1 LPL spectra of a nanocrystalline CeO<sub>2</sub> thin film annealed at 800 °C at an OFR of 50 sccm, measured at 10, 15, 18 and 22 Kelvin (K).

Figure 1  
[Click here to download high resolution image](#)

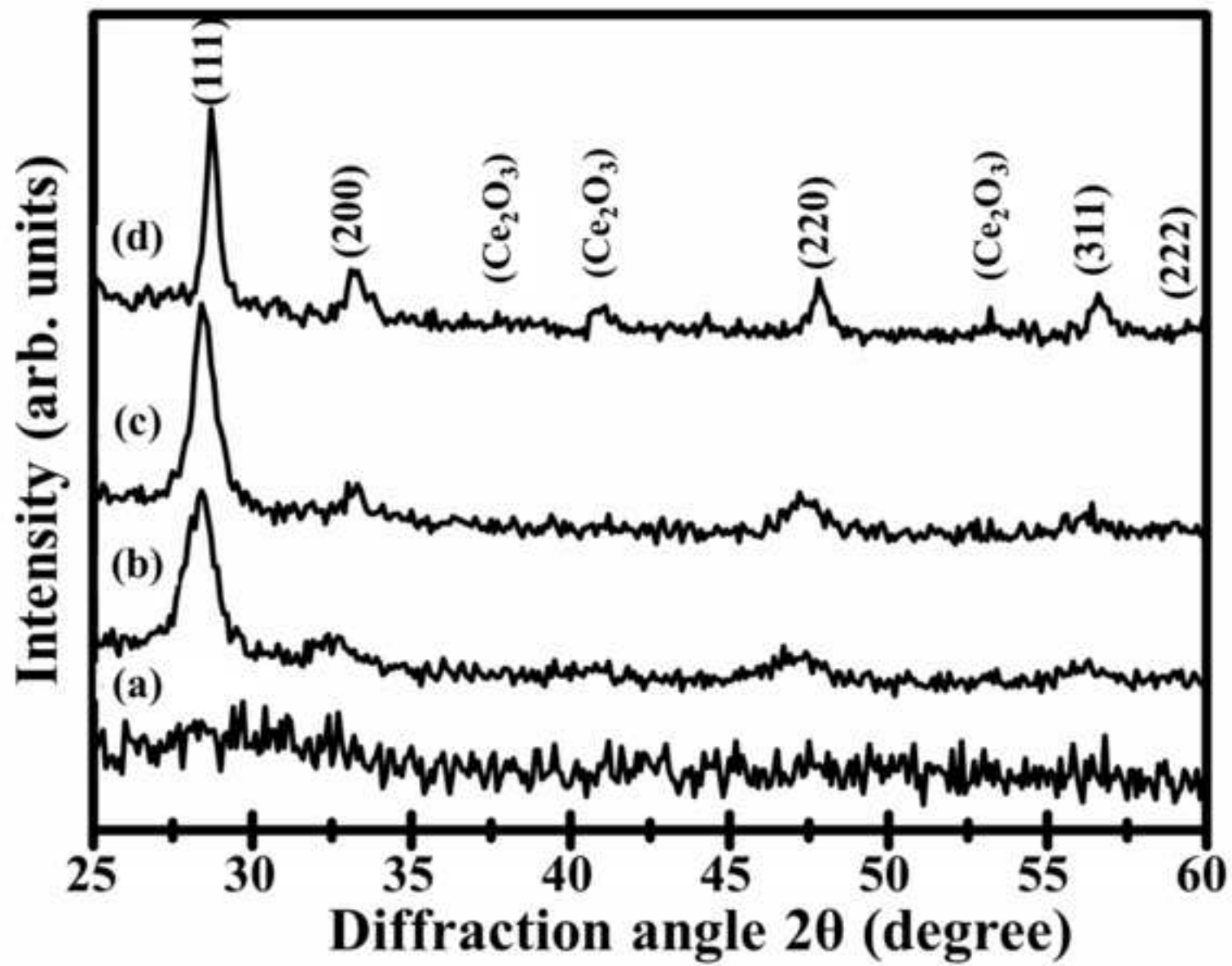


Figure 2a

[Click here to download high resolution image](#)

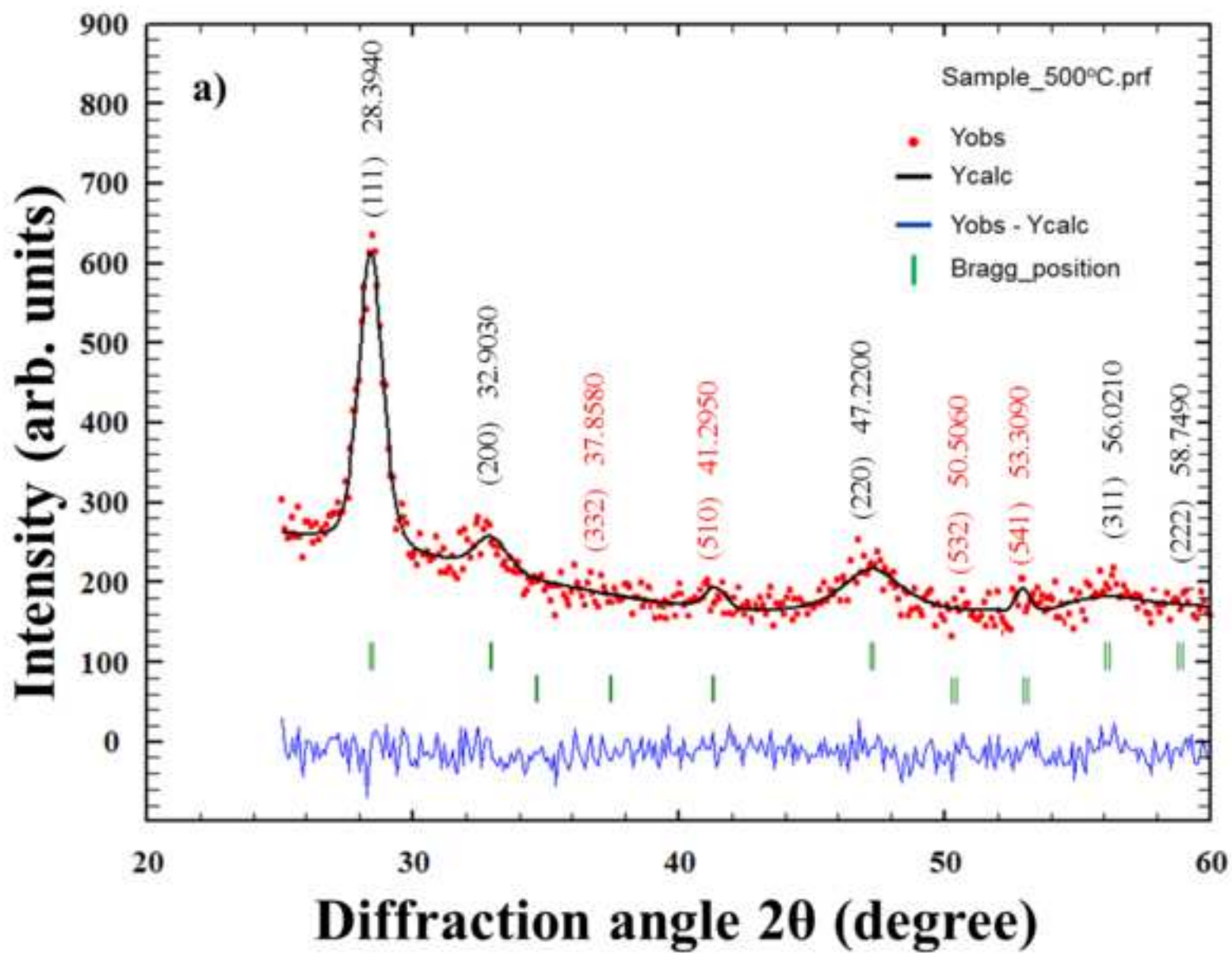


Figure 2b

[Click here to download high resolution image](#)

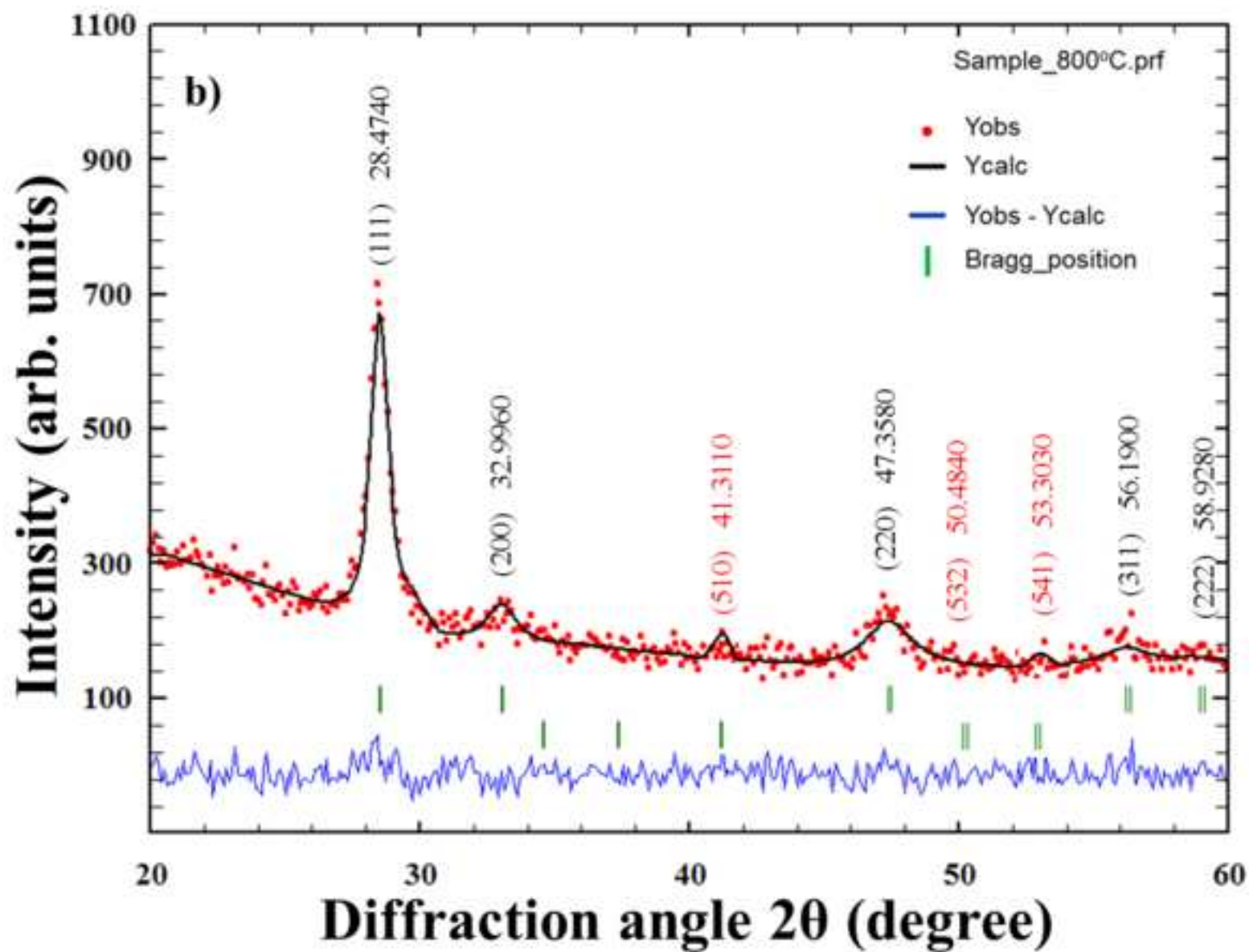


Figure 2c

[Click here to download high resolution image](#)

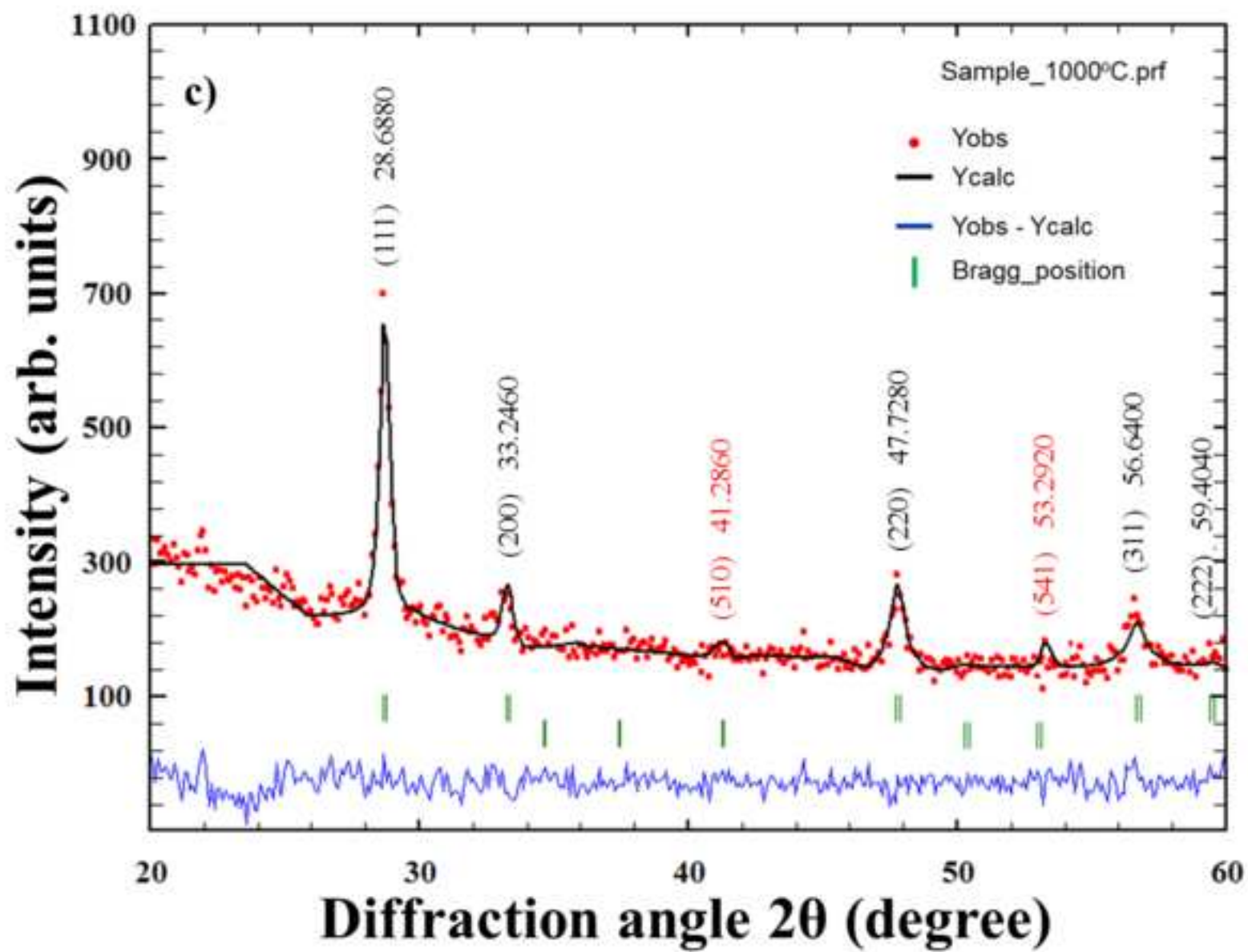


Figure 3  
[Click here to download high resolution image](#)

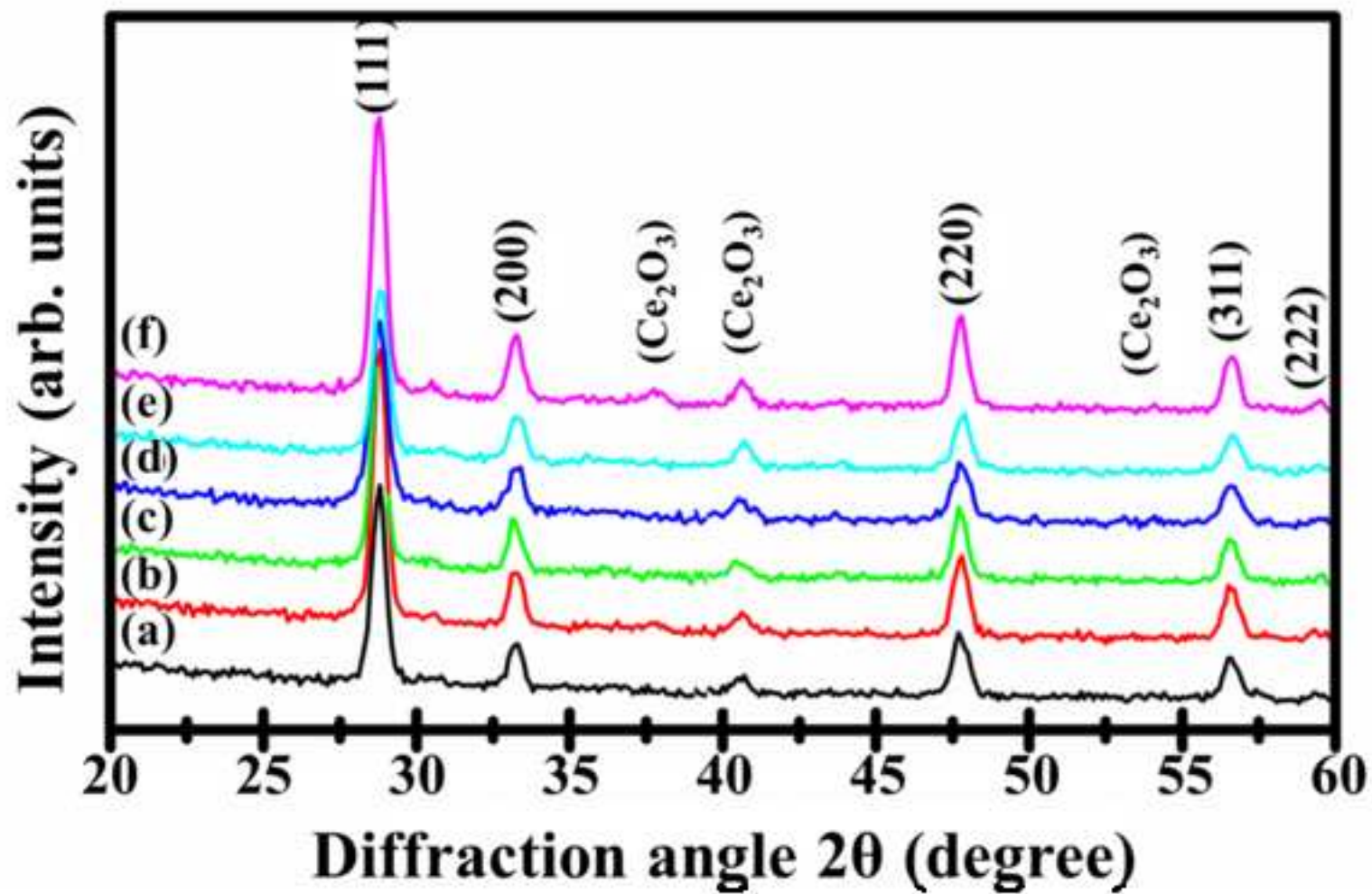


Figure 4  
[Click here to download high resolution image](#)

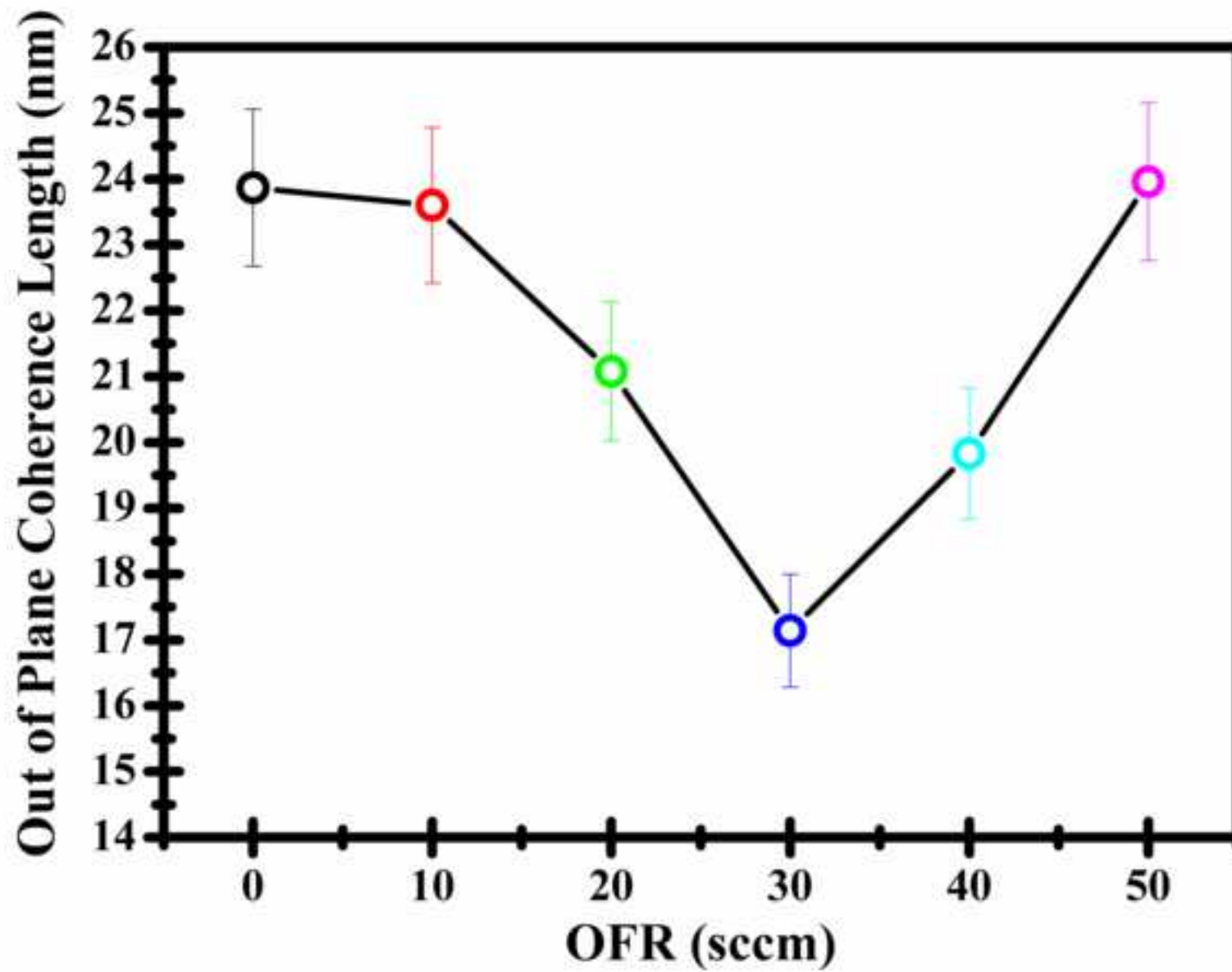


Figure 5a  
[Click here to download high resolution image](#)

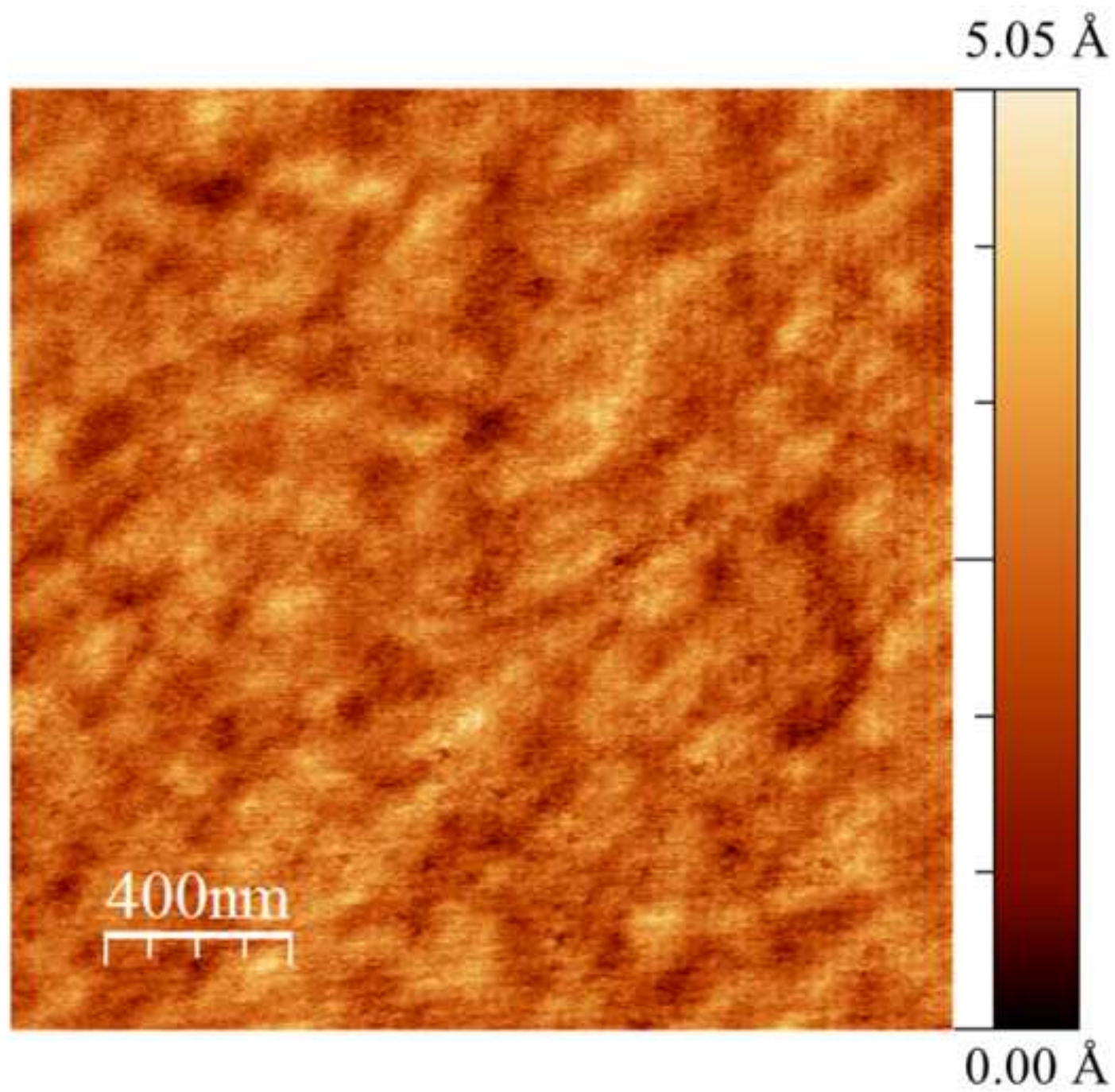


Figure 5b  
[Click here to download high resolution image](#)

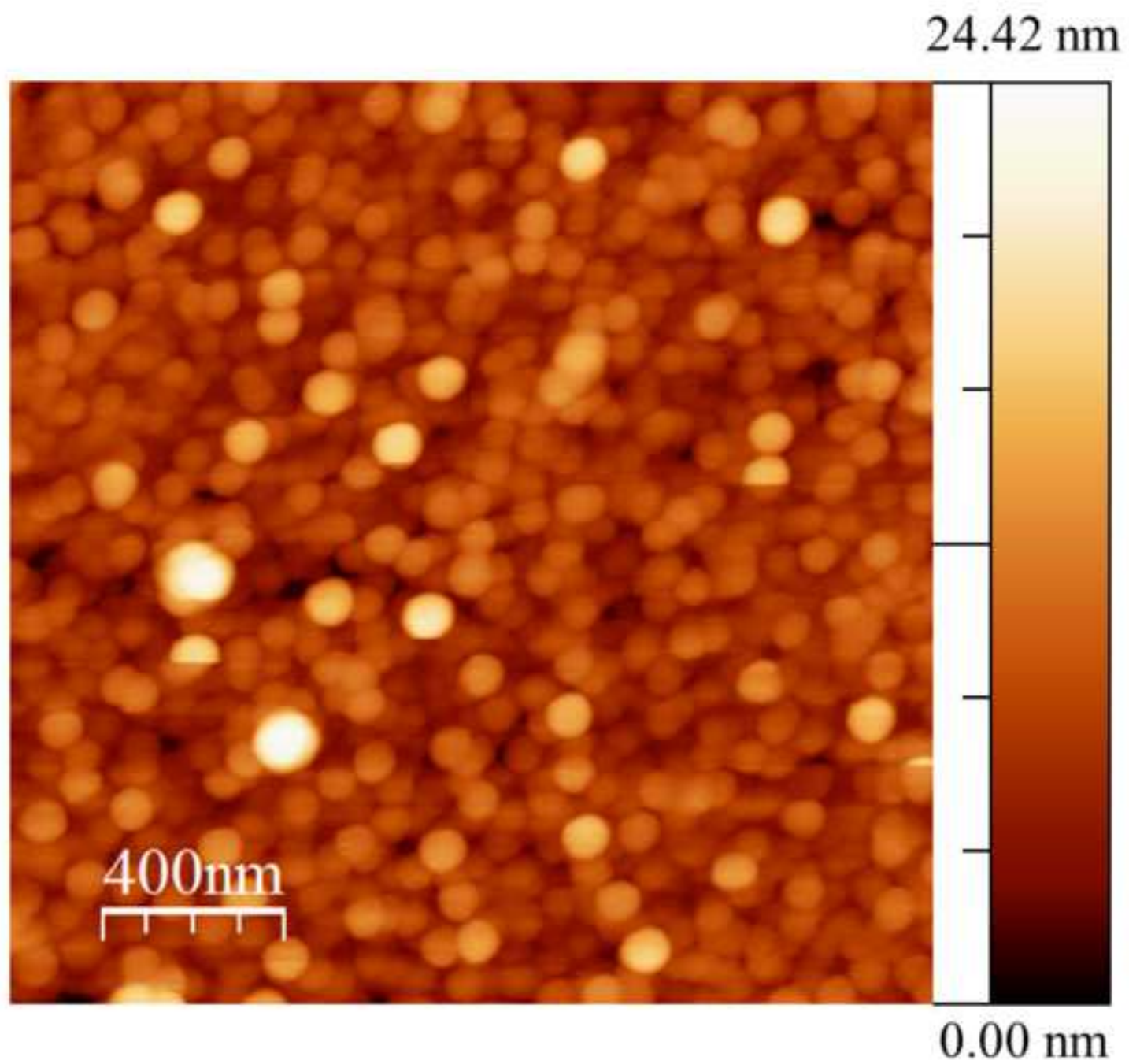


Figure 5c  
[Click here to download high resolution image](#)

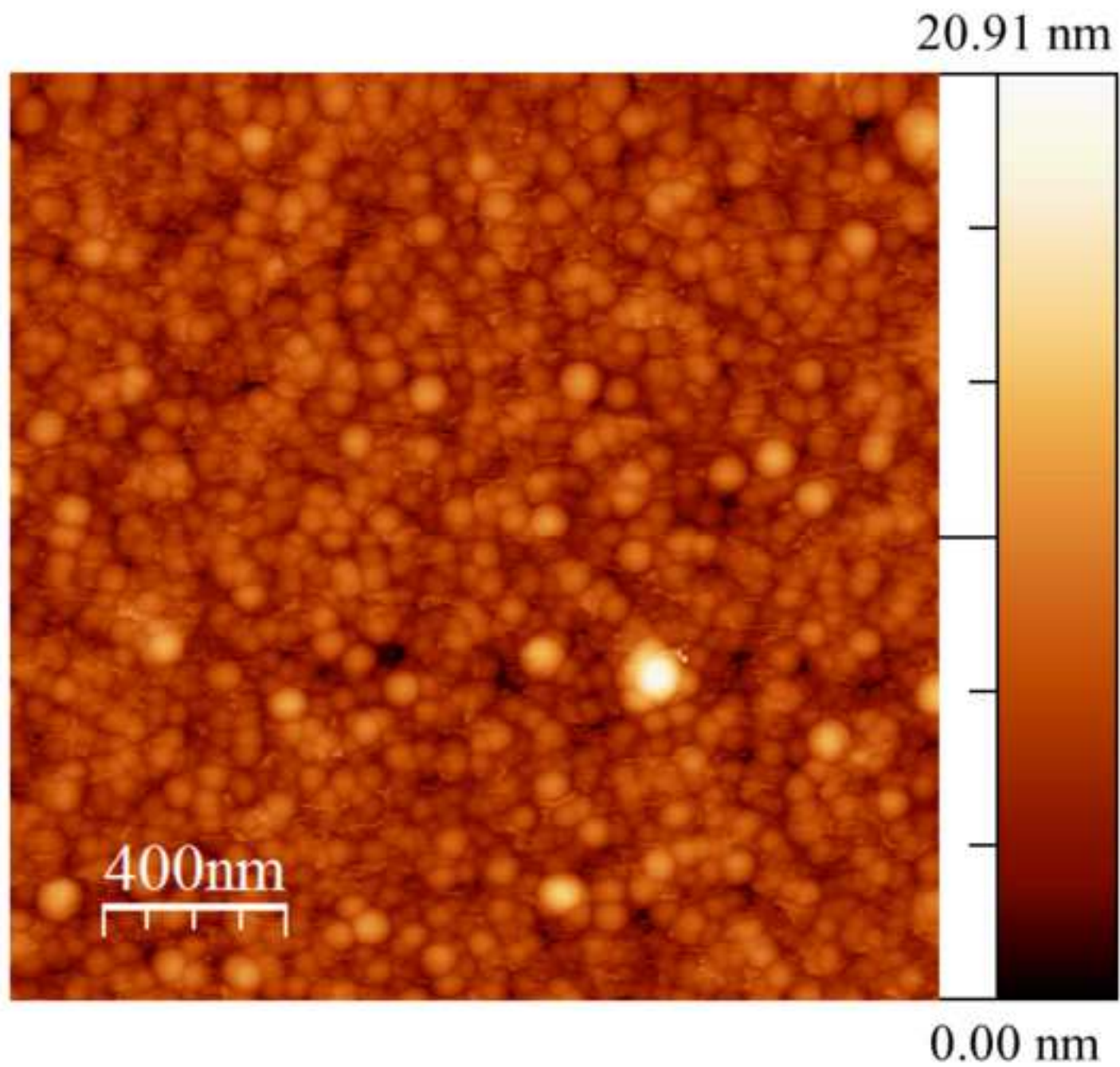


Figure 5d  
[Click here to download high resolution image](#)

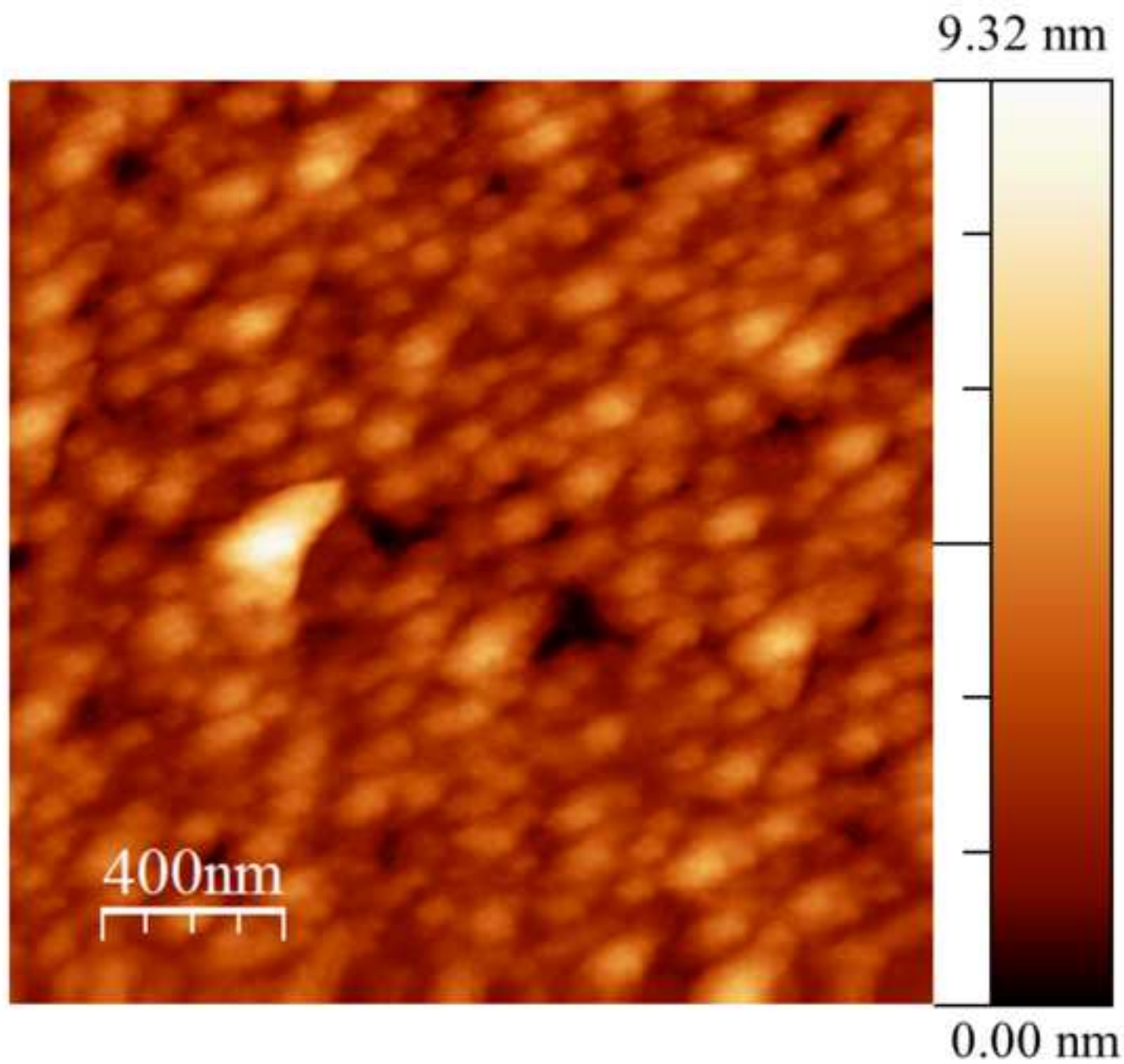


Figure 5e  
[Click here to download high resolution image](#)

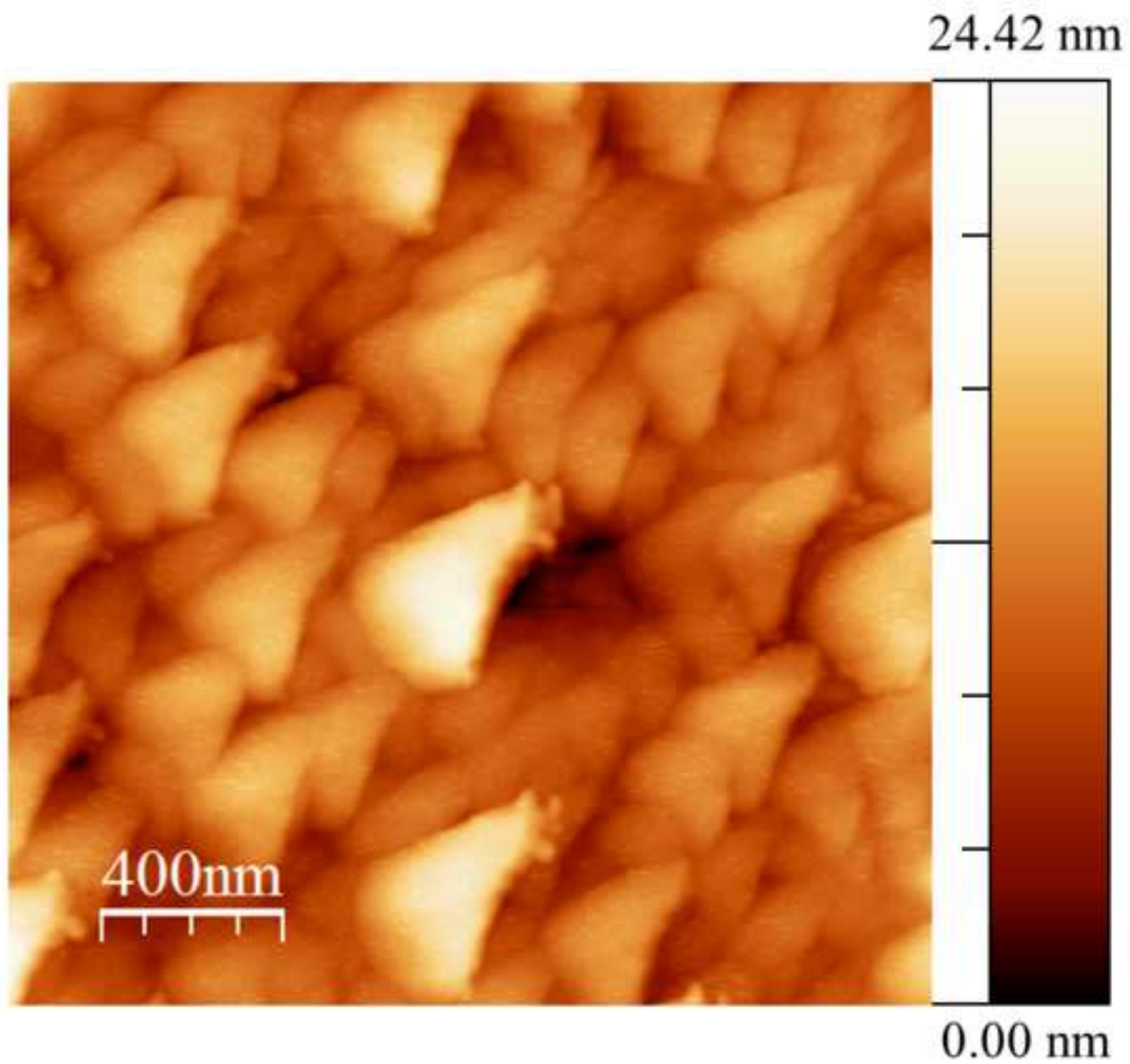


Figure 6  
[Click here to download high resolution image](#)

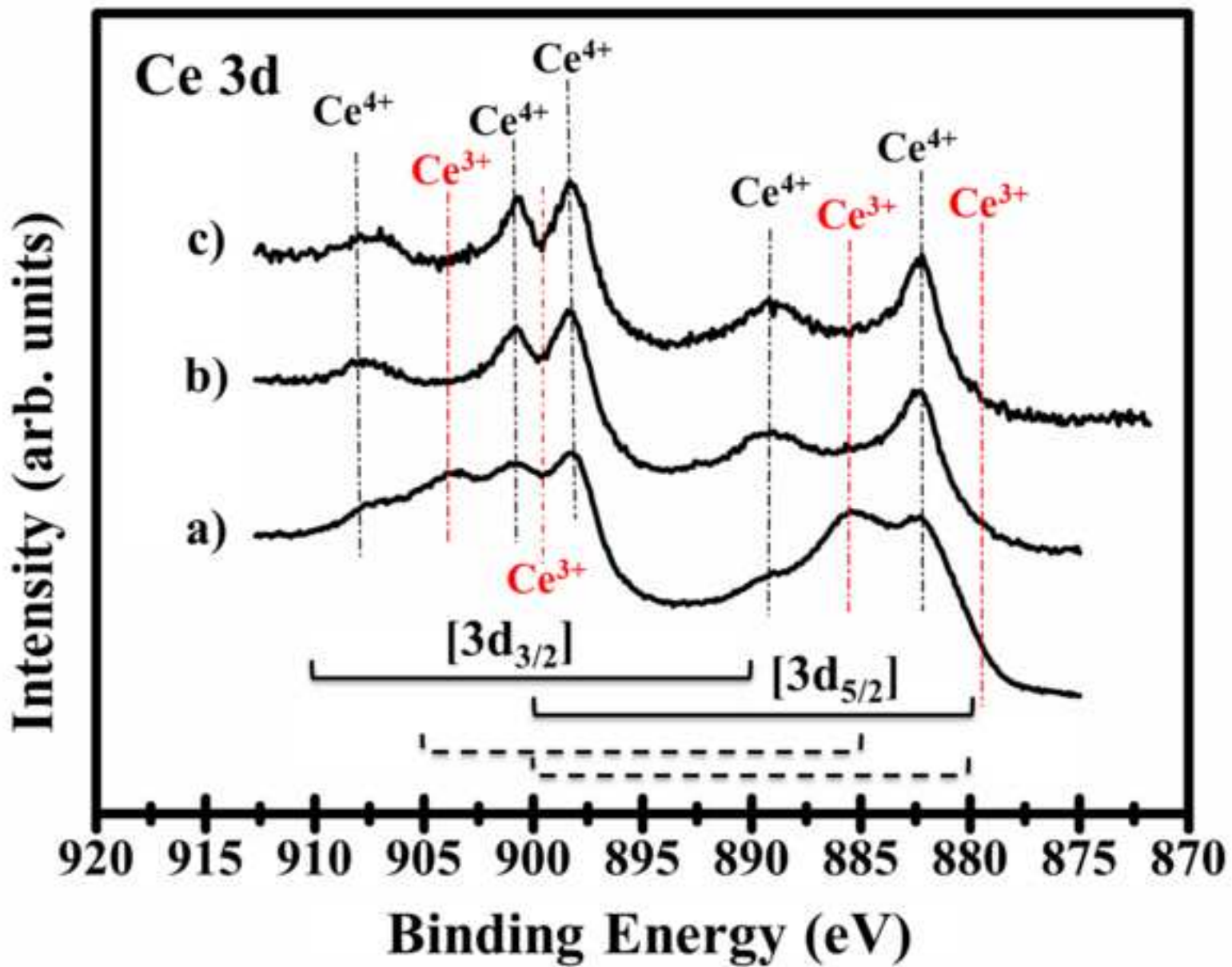


Figure 7  
[Click here to download high resolution image](#)

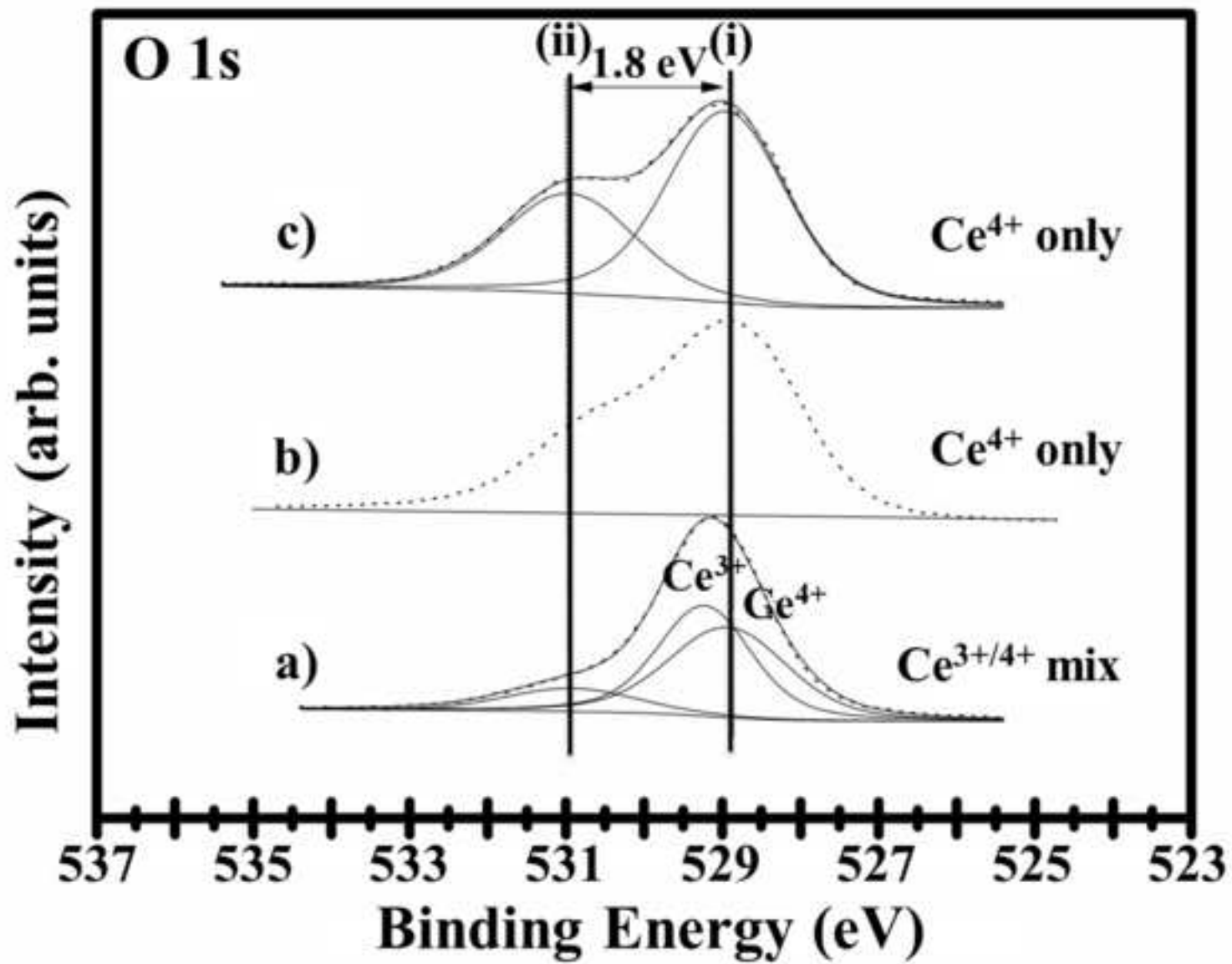


Figure 8  
[Click here to download high resolution image](#)

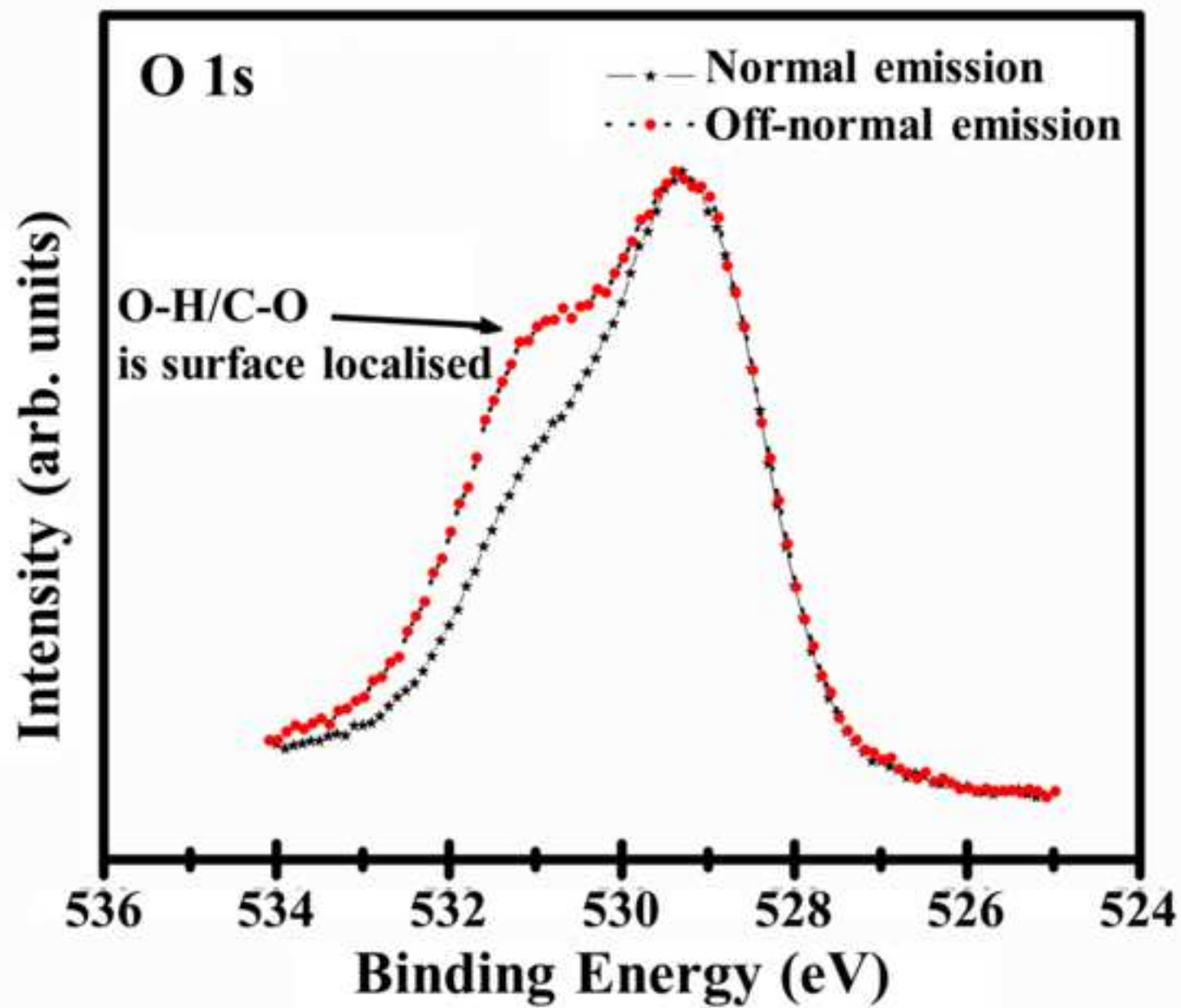


Figure 9  
[Click here to download high resolution image](#)

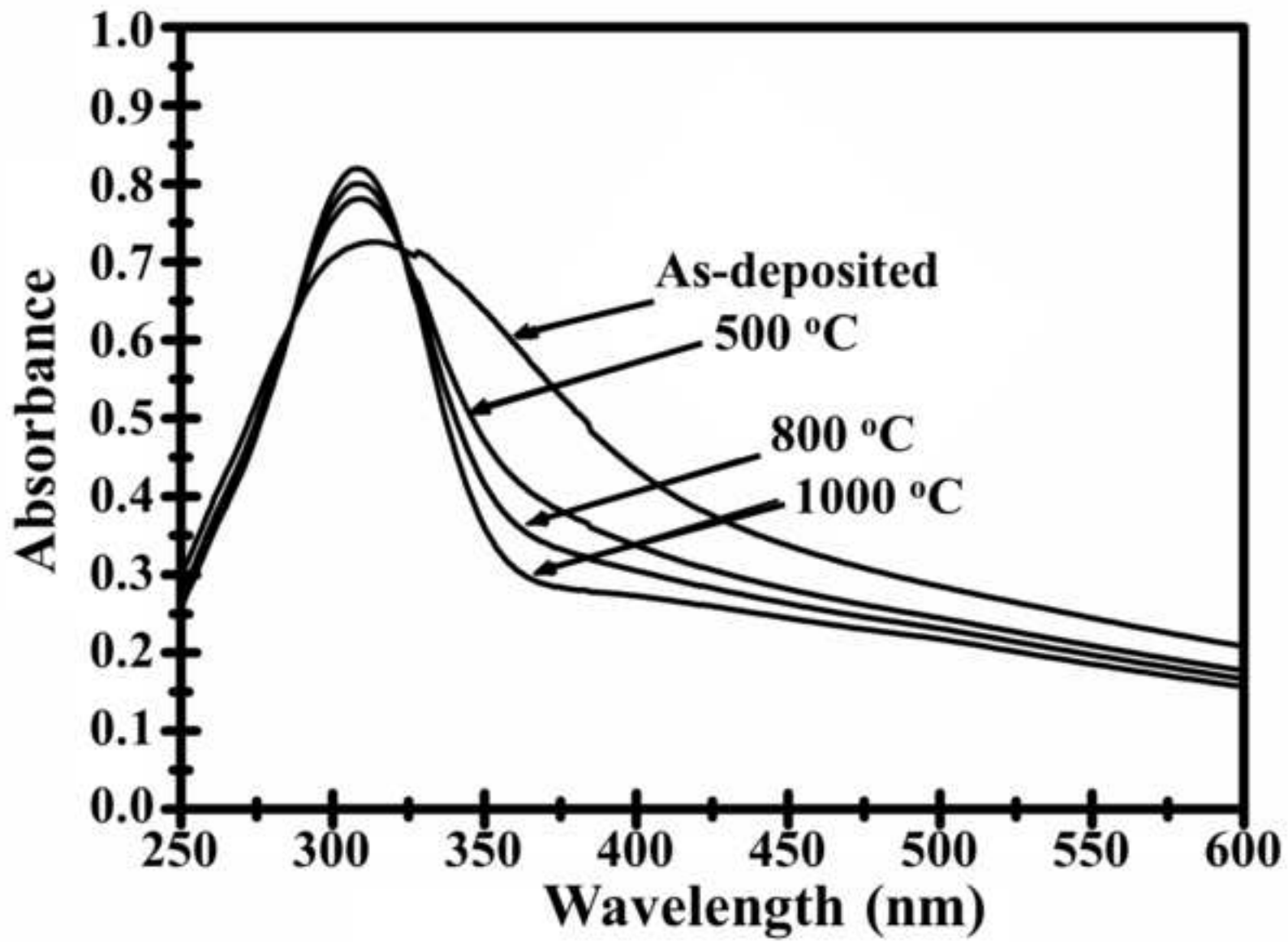


Figure 10  
[Click here to download high resolution image](#)

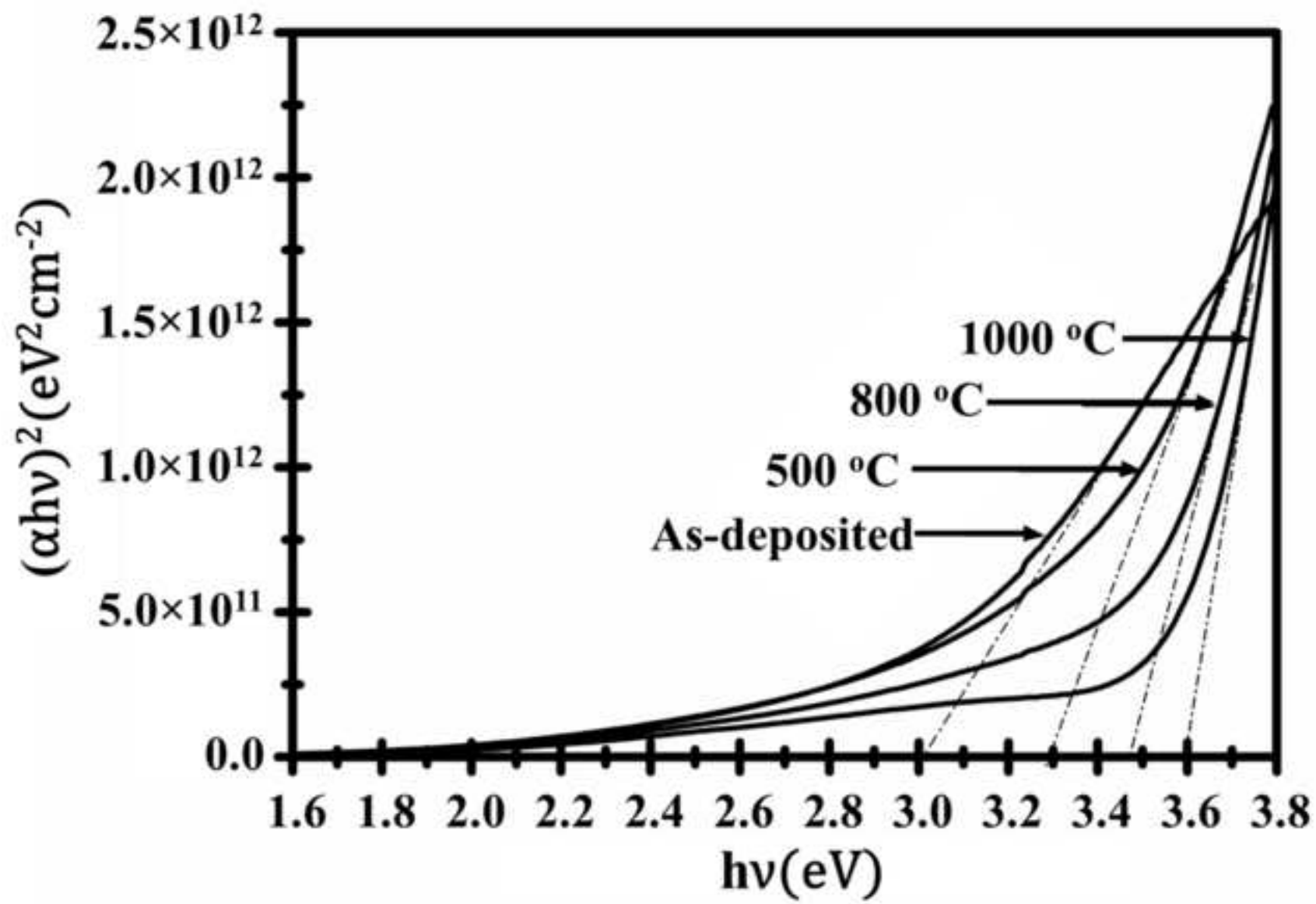


Figure 11  
[Click here to download high resolution image](#)

